Mon. Not. R. Astron. Soc. **000**, 1–?? (2015) Printed 5 January 2016 (MN LATEX style file v2.2)

Gravitational collapse and the thermal evolution of low-metallicity gas clouds in the early Universe

Gen Chiaki,[1⋆] Naoki Yoshida[1,2] and Shingo Hirano[1]
[1] *Department of Physics, Graduate School of Science, University of Tokyo, 7-3-1 Hongo, Bunkyo, Tokyo 113-0033, Japan*
[2] *Kavli Institute for the Physics and Mathematics of the Universe (WPI), Todai Institutes for Advanced Study, The University of Tokyo, Kashiwa, Chiba 277-8583, Japan*

ABSTRACT

We study gravitational collapse of low-metallicity gas clouds and the formation of protostars by three-dimensional hydrodynamic simulations. Grain growth, non-equilibrium chemistry, molecular cooling, and chemical heating are solved in a self-consistent manner for the first time. We employ the realistic initial conditions for the abundances of metal and dust, and the dust size distribution obtained from recent Population III supernova calculations. We also introduce the state-of-the-art particle splitting method based on the Voronoi tessellation and achieve an extremely high mass resolution of $\sim 10^{-5}$ $M_\odot$ (10 earth masses) in the central region. We follow the thermal evolution of several early clouds with various metallicities. We show that the condition for cloud fragmentation depends not only on the gas metallicity but also on the collapse timescale. In many cases, the cloud fragmentation is prevented by the chemical heating owing to molecular hydrogen formation even though dust cooling becomes effective. Meanwhile, in several cases, efficient OH and H_2O cooling promotes the cloud elongation, and then cloud "filamentation" is driven by dust thermal emission as a precursor of eventual fragmentation. While the filament fragmentation is driven by rapid gas cooling with $\gtrsim 10^{-5}$ $Z_\odot$, fragmentation occurs in a different manner by the self-gravity of a circumstellar disk with $\lesssim 10^{-5}$ $Z_\odot$. We use a semi-analytic model to estimate the number fraction of the clouds which undergo the filament fragmentation to be a several percents with 10^{-5}–10^{-4} $Z_\odot$. Overall, our simulations show a viable formation path of the recently discovered Galactic low-mass stars with extremely small metallicities.

Key words: dust, extinction — galaxies: evolution — ISM: abundances — stars: formation — stars: low-mass — stars: Population II

1 INTRODUCTION

The origin of Galactic extremely metal-poor stars remains largely unknown. Their small metal content suggests that they were born very early, while their small masses pose interesting questions on star formation in a metal-poor environment. For example, the star SDSS J102915 + 172927 with the mass 0.8 $M_\odot$ has an extremely low metallicity of 4.5×10^{-5} $Z_\odot$ (Caffau et al. 2011b, 2012), and thus is thought to be one of the second generation stars; it was probably born in a gas cloud that had been enriched with heavy elements synthesized by the first generation of stars (Pop III stars).

Recent theoretical studies based on cosmological hydrodynamic simulations suggest that the first generation stars formed from a metal-free, primordial gas have a wide range of masses (Hirano et al. 2014; Susa et al. 2014). Such a notion is supported by observations of metal-poor stars whose peculiar abundance patterns are consistent with the nucleosynthetic models of massive primordial stars (Caffau et al. 2011b; Keller et al. 2014). Interestingly, the recently discovered star SDSS J001820.5 − 093939.2 shows characteristic signatures of the metal yield of a very massive primordial star, suggesting a broad mass distribution of the Pop III stars (Aoki et al. 2014).

A trace amount of heavy elements in a star-forming gas plays an important role in the formation of the low-mass stars with extremely low metallicities (Omukai 2000; Bromm & Loeb 2003; Schneider et al. 2003). Efficient gas cooling owing to metal and dust can trigger the cloud fragmentation. In general, gas cooling promotes the cloud deformation into sheets or filaments, whereas heating processes

⋆ E-mail: gen.chiaki@utap.phys.s.u-tokyo.ac.jp

stabilize the gas against aspherical perturbations. The linear analyses by Lai (2000) and Hanawa & Matsumoto (2000) demonstrate that a contracting cloud gets highly elongated when the specific heat ratio $\gamma = \mathrm{d}\ln T/\mathrm{d}\ln\rho + 1$, an indicator of the effective gas equation of state, is less than 1.1. In a cooling gas with $\gamma < 1$, significantly elongated filamentary structures tend to be formed. When the density of the filament increases up to a value where gas cooling becomes insufficient ($\gamma > 1$), multiple cores are formed and begin contracting separately. Therefore, the characteristic mass of the fragments is set by the Jeans mass at the density and temperature where the cooling becomes inefficient. Analytic models suggest that low-mass cores can be formed by transition line cooling of C I, C II, and O I (Bromm & Loeb 2003; Frebel et al. 2005; Santoro & Shull 2006; Ji et al. 2014). Dust thermal emission is another important process that determine the thermal evolution of a low-metallicity gas. A semi-analytic approach reveals that dust cooling becomes important at densities $n_{\rm H} \gtrsim 10^{12}$ cm^{-3}, where the corresponding Jeans mass is $\sim$ 0.1 M$_\odot$ (Omukai 2000; Schneider et al. 2003).

Three-dimensional hydrodynamic simulations have been also performed to study the conditions for gas cloud fragmentation and for the formation of low-mass stars. Dopcke et al. (2011, 2013) follow the dynamical evolution of a turbulent gas with metallicities below 10^{-4} Z$_\odot$. They show that several tens of sink particles are formed in the gas and that the mass distribution of the sink particles becomes from flat to peaky distribution with increasing metallicity. Safranek-Shrader et al. (2014a,b) perform simulations with a proper cosmological set-up to investigate star formation in dense clumps in early galaxies with gas metallicities of 10^{-4}–10^{-2} Z$_\odot$. They find that the gas fragments into sink particles, whose mass distribution is consistent with the observationally derived stellar masses of the ultra faint dwarf spheroidal galaxies. More recently, Smith et al. (2015) study the effects of metal pollution and turbulence driven by a Pop III supernova explosion into the neighboring halo. The gas polluted to metallicity of 2×10^{-5} Z$_\odot$ fragments by dust thermal emission. Their study explicitly includes the process of the dispersion of metals and dust.

These previous studies assume the metal abundances, grain condensation efficiency, and the dust size distribution to be those in the Galactic interstellar medium despite the fact that the metal-poor stars observed so far show peculiar abundance patterns. For example, the abundance ratio of light elements such as carbon and oxygen relative to iron is enhanced with respect to the solar value (Suda et al. 2008; Tominaga et al. 2014). Because the efficiency of metal line cooling is determined by the abundance of respective elements, it is important to adopt realistic values based on, for example, the nucleosynthesis calculations of Pop III supernovae.

The same is true for the condensation efficiency, or the mass fraction of heavy elements condensed into dust grains. It is known that a significant fraction of heavy elements are locked into dust grains in the local interstellar medium (Pollack et al. 1994), but recent spectroscopic observations of damped Lyman-α systems with metallicity $\sim 10^{-3}$ Z$_\odot$ suggest that the condensation efficiency is smaller at redshifts $z \sim 6$ (Schady et al. 2010; Zafar et al. 2011). It is also known that grain growth, i.e., accretion of the gas-phase metals onto dust grains, can enhance the dust cooling efficiency in a collapsing cloud even with an extremely low metallicity to be close to that of the local interstellar medium (Nozawa et al. 2012; Chiaki et al. 2013).

There are other important processes in a low-metallicity gas that have often been overlooked in previous studies. O- and C-bearing molecules such as OH and H_2O act as important coolants at intermediate densities $n_{\rm H} \sim 10^4$–10^8 cm^{-3}. Although OH and H_2O cooling is less effective in a gas with the "normal" elemental composition (Omukai 2000), our previous work (Chiaki et al. 2015, hereafter C15) reveals that the molecular cooling is efficient in some cases when the realistic initial condition (composition) is adopted. There is yet another important heating process. When hydrogen molecules are formed, the binding energy is released to be converted into the gas kinetic energy. Tsuribe & Omukai (2008) argue that the gas heating can stabilize the gas to prevent fragmentation using simulations of a polytropic gas mimicking the thermal evolution of low-metallicity clouds.

The metal and dust properties in the early Universe can be determined theoretically under the assumption that the formation sites of low-metallicity stars are in clouds partly polluted with metals and dust by Pop III supernovae in the same or nearby halos (Ritter et al. 2012; Smith et al. 2015). Thus, the abundances of heavy elements and dust species, and the dust size distribution are expected to be set by the nucleosynthetic process of the supernova explosion (Umeda & Nomoto 2002) and the dust formation and destruction history during propagation of blast waves (Todini & Ferrara 2001; Nozawa et al. 2003; Schneider et al. 2006).

In the present paper, we perform hydrodynamic simulations of collapsing gas clouds with various metallicities 10^{-6}–10^{-3} Z$_\odot$. We study in detail the critical conditions for gas fragmentation and for the formation of low-mass protostars. Our three-dimensional simulations follow, for the first time, all the necessary thermal processes including dust thermal emission, gas heating by H_2 formation, and OH and H_2O cooling. The metal abundances, initial grain condensation efficiency, and the dust size distribution are calculated in the stellar evolution and supernova explosion models of a Pop III star. We calculate the chemical reactions and grain growth in a direct, self-consistent manner in order to compute the cooling and heating rates. Recently, Hirano et al. (2014) find that the different collapse timescales of the primordial star-forming cloud gives the wide mass distribution of Pop III stars, $\sim$ 10–1000 M$_\odot$. In this paper, we employ four gas clouds with different collapse timescales to examine the effect of the cloud variation on the low-metal star formation.

2 NUMERICAL SIMULATIONS

2.1 Chemistry and cooling

We use the parallel N-body/smoothed particle hydrodynamics (SPH) code GADGET-2 (Springel 2005) with non-equilibrium chemistry and radiative cooling. We solve chemical networks of 54 reactions for 27 gas-phase species: H^+, e^-, H, H^-, H_2, D^+, D, HD, C^+, C, CH, CH_2, CO^+, CO, CO_2, O^+, O, OH^+, OH, H_2O^+, H_2O, H_3O^+, O_2^+, O_2, Si,

SiO, and SiO_2. The chemical reaction rates are given in C15 for Si-bearing species, and in Omukai et al. (2010) for other species. We solve the chemical reactions implicitly to obtain the abundances of the gas-phase species in each fluid element at each time step. We then calculate the associated cooling and heating rates.

We implement radiative cooling by C^+, C, and O, and by H_2 and HD molecules. We calculate the level populations for each species in a time-dependent manner. Gas opacity is explicitly calculated and the cooling rate for each emission line is reduced by a factor determined by the local velocity gradient in the optically thick regime (the so-called Sobolev approximation). We calculate the velocity gradient in the three directions x, y, and z as in Hirano & Yoshida (2013). We also include metal molecular line cooling, using the formulation and the cooling tables presented by Neufeld & Kaufman (1993) and Neufeld et al. (1995) for H_2O and Omukai et al. (2010) for CO and OH. We obtain the cooling rate $\Lambda_i(m)$ of molecules m = CO, OH, and H_2O with the column density $\tilde{N}(m) = n(m)|dv_i/dr_i|$ in the three directions $i = x$, y, and z, and take the average as $\Lambda(m) = [\Lambda_x(m) + \Lambda_y(m) + \Lambda_z(m)]/3$.

Hydrogen molecules are formed via endothermic reactions with $E = 4.48$ eV per formed molecule. The three-body reactions particularly enhance the temperature at densities 10^8–10^{11} cm^{-3}. Tsuribe & Omukai (2008) find that the gas heating resulting from the rapid hydrogen molecular formation mitigates the cloud deformation and makes the cloud core rounder. We consider the heating mechanism according to the formulation of Hollenbach & McKee (1979) and Omukai (2000).

2.2 Grain growth

The dust species considered here are metallic silicon (Si), metallic iron (Fe), forsterite (Mg_2SiO_4), enstatite ($MgSiO_3$), amorphous carbon (C), silica (SiO_2), magnesia (MgO), troilite (FeS), and alumina (Al_2O_3). We follow the evolution of the size distributions and abundances of the grain species by essentially treating the grain growth as chemical reactions. We consider 13 reactions as in C15. We integrate the growth rate (Equation (9) in C15) to derive the grain radius and condensation efficiency at each time for each fluid element. We then calculate the reaction rate of hydrogen molecular formation on grain surfaces, radiative cooling efficiency, and continuum opacity for every grain species and radius. The optical depth to continuum emission is estimated as $\tau_{\rm cont} = \kappa\rho\lambda_{\rm J}$, where κ is the total absorption cross section of gas and dust per unit fluid mass, ρ is the total density of gas and dust, and $\lambda_{\rm J}$ is the local Jeans length.

2.3 Particle splitting

We need to follow the gas cloud collapse to very high densities. The Jeans length of the central, densest part decreases eventually down to ~ 0.1 AU when a protostellar core is formed. To save the computational cost, we use the particle splitting technique, when the resolution is about to violate the Jeans criterion (Truelove et al. 1997, 1998). Dense gas particles are replaced with less massive daughter particles. In Chiaki & Yoshida (2015), we present a novel method in which the daughter particles are distributed based on the Voronoi diagram tessellated by parent particles. With this method, the density structures of the cloud is well preserved. In the entire course of our simulations, a Jeans mass is required to be resolved by more than $1000M_{\rm min}$, where $M_{\rm min} = N_{\rm ngb}m_{\rm p}$ is the minimal resolvable mass of the parent SPH particles with mass $m_{\rm p}$, and $N_{\rm ngb}$ is the number of the neighbor particles. We set $N_{\rm ngb} = 64 \pm 8$, and thus the Jeans mass is always resolved by $\sim 10^5$ particles.

2.4 Later accretion phase

As the density in the central core increases, the dynamical time decreases and the necessary integration time step gets progressively shorter. Sink particle techniques are often employed to save computational time, where the gas inside a pre-determined accretion radius is replaced with a sink particle (Dopcke et al. 2013; Safranek-Shrader et al. 2014b; Smith et al. 2015). The evolution of a circumstellar disk, through which the gas is accreted, is not followed accurately with sink particle techniques. It is also known that the separation of fragments depends on the accretion radius (Machida & Doi 2013; Greif et al. 2012). Instead of employing a sink particle technique, we resort to following the gas dynamics in and around the proto-stellar core by setting the specific heat ratio to be $\gamma = 1.4$ after the density of fluid elements exceeds $n_{\rm H} = 10^{16}$ cm^{-3}, where the gas becomes optically thick even in a primordial gas. Although we are not able to follow the thermal evolution accurately beyond $n_{\rm H} = 10^{16}$ cm^{-3}, the treatment allows us to examine gas fragmentation owing to dust thermal emission, which is expected to be effective at $n_{\rm H} \gtrsim 10^{12}$–$10^{15}$ cm^{-3}.

2.5 Initial conditions

2.5.1 Cloud models

We use two different sets of initial conditions; one spherical cloud as a controlled simulation, and three clouds hosted by small dark matter halos selected from cosmological simulations. The spherical cloud has a uniform density $n_{\rm H,ini} = 0.1$ cm^{-3} and temperature $T_{\rm ini} = 300$ K. The cloud radius and mass are $R_{\rm ini} = 551$ pc and $M_{\rm ini} = 2.3 \times 10^6$ M$_\odot$, corresponding to the half Jeans length and the Jeans mass, respectively, for the uniform cloud with density $n_{\rm H,ini}/f_{\rm enh}$, where $f_{\rm enh} = 1.8$ is the enhancement factor (Matsumoto & Hanawa 2003). We perturb the initial densities so that the root mean square of the density is 10% of the mean density. We impose solid rotation such that the rotation energy relative to the gravitational energy $\beta_{\rm ini} = \Omega_{\rm ini}^2 R_{\rm ini}^3/3GM_{\rm ini}$ is 10^{-3}, corresponding to the angular velocity $\Omega_{\rm ini} = 1.4 \times 10^{-17}$ s^{-1}. The initial number fractions of deuterium and helium relative to hydrogen nuclei are 5.3×10^{-5} and 0.079, respectively. The number fractions of electron and hydrogen molecules relative to hydrogen nuclei are $y(e) = 10^{-4}$ and $y(H_2) = 10^{-6}$, respectively. Both deuterium and helium are initially assumed to be in neutral atoms. The spherical cloud calculations are dubbed "UNI" hereafter.

We also perform collapse simulations for gas clouds hosted by minihalos chosen from the cosmological simulations of Hirano et al. (2014). From the large simulation box

Table 1. Abundances of heavy elements

X	C	O	Mg	Al	Si	S	Fe
A_X	1.08×10^{-4}	1.19×10^{-3}	4.19×10^{-5}	8.29×10^{-7}	6.67×10^{-5}	3.01×10^{-5}	6.76×10^{-6}
[X/Fe]	0.22	1.01	0.77	0.14	0.99	1.01	0.00

Note — Abundances of heavy elements released by a Pop III supernova with progenitor mass 30 $M_\odot$ in an ambient gas with density $n_{\rm amb} = 1$ cm^{-3} (Nozawa et al. 2007). We show the number abundances relative to hydrogen nuclei with metallicity $Z = Z_\odot$. The values are reduced by the factor $Z/Z_\odot$ for metallicity Z. In the second row, the relative abundance $[X/{\rm Fe}] = \log(A_X/A_{\rm Fe}) - \log(A_{X,\odot}/A_{{\rm Fe},\odot})$ is shown. The solar abundance $A_{X,\odot}$ is taken from Caffau et al. (2011a).

Table 2. Properties of grains

i	Silicon	Iron	Forsterite	Enstatite	Carbon	Silica	Magnesia	Troilite	Alumina	Total
$f_{{\rm dep},i,0}$ [$\times 10^{-3}$]	29.14	1.93	0.77	< 0.01	0.62	5.27	1.34	0.45	< 0.01	39.53
$r_{i,0}^{\rm grow}$ [$\times 10^{-2}$ μm]	38.67	28.30	1.20	1.38	1.97	5.76	5.31	3.53	0.11	

Note — Initial depletion factor $f_{{\rm dep},i,0}$ relative to total mass of metal and dust and the characteristic radius $r_{i,0}^{\rm grow} = \langle r^3 \rangle_i / \langle r^2 \rangle_i$ of grain species i.

of ~ 1 Mpc on a side, we cut out the region centered at a minihalo with radii ~ 1 kpc so that sound waves cannot cross the region during the cloud collapse. We select three minihalos dubbed "MH1", "MH2", and "MH3", which cover the different types of the early clouds. In the simulations performed by Hirano et al. (2014) for the three clouds without metal, the masses of the hosted Pop III stars are 283.9, 751.3, and 60.5 $M_\odot$, respectively. The thermal evolution differs from cloud to cloud, and probably affects the resulting fragmentation properties as discussed in Appendix C of Hirano et al. (2014).

2.5.2 Metal and dust properties

In our simulations, metals and dust are uniformly added to the simulation gas particles. The metal abundance, dust condensation efficiency, and dust size distribution are taken from a model of nucleosynthesis and grain formation/destruction in a Pop III supernova. For the first time, we adopt such the realistic initial conditions to the three-dimensional simulations of the Pop II star formation, while previous works often assume the solar abundance pattern. We employ a Pop III supernova model with the progenitor mass 30 $M_\odot$ and the ambient gas density $n_{\rm amb} = 1$ cm^{-3} taken from Nozawa et al. (2007) as a characteristic model. Tables 1 and 2 show the metal and dust properties, respectively.

We briefly summarize the difference between the Pop III supernova model and the present-day model. First, the number fractions of the light elements relative to iron are larger in the latter case (second row of Table 1). In particular, the Pop III model predicts a large fraction of [O/Fe] $\simeq 1$. We thus expect that the radiative cooling by OH and H_2O molecules is more efficient than in the case of solar abundance. Second, the total condensation efficiency of metal is only 4%, which is much smaller than $\sim 50\%$ in the present-day. Although the grain growth can enhance the final dust-to-gas mass ratio, the efficiency of H_2 formation on grains and dust cooling rate are still smaller than in the present-day case.

The Pop III supernova model gives us the relative abundances of metal and dust. Their absolute values are determined for a given metallicity, or the total mass fraction of heavy element to the gas. We examine four cases with metallicities 10^{-6}, 10^{-5}, 10^{-4}, and 10^{-3} times the solar value $Z_\odot = 0.02$. Hereafter we call the models as Z6, Z5, Z4, and Z3, respectively. We assume that initially all of C nuclei are in the form of C^+, and O and Si are in neutral atoms. The initial mass fraction $f_{{\rm dep},i,0}$ of grain species i relative to metal and the characteristic radius of grains (see C15) are shown in Table 2.

3 CHEMO-THERMAL EVOLUTION OF SPHERICAL CLOUDS

Particle splitting allows us to follow the nonlinear gravitational evoltution from a diffuse interstellar cloud to protostellar core(s) over 20 orders of magnitude in density. The mass resolution $M_{\rm min}$ is initially 320 $M_\odot$ and eventually reaches 3.2×10^{-5} $M_\odot$ (10 Earth masses) in the central densest region with $\gtrsim 10^{16}$ cm^{-3} after splitting particles seven times.

Figure 1 shows the temperature evolution as a function of density of the core in UNI simulations for Z3–6.[1] Figure 2 shows the evolution of the gas cooling and heating rates, and the abundances of Si-bearing species and grains as a function of the central density for UNI Z5.

Adiabatic compressional heating is dominant for all the cases at densities $\lesssim 1$ cm^{-3}. After that, molecular hydrogen cooling becomes important until the density reaches the critical value for H_2 molecules, $n_{\rm H} \sim 10^3$ cm^{-3}, where the level population is set by the LTE one. For Z4–6, the temperature increases only slowly by the balance between the gas

[1] Hereafter, we measure the quantities such as the temperature, density, chemical abundance, and cooling rate in the central region by mass-weighting over the gas particles with densities $n_{\rm H} > n_{\rm H,peak}/3$, where $n_{\rm H,peak}$ is the largest density in each snapshot.

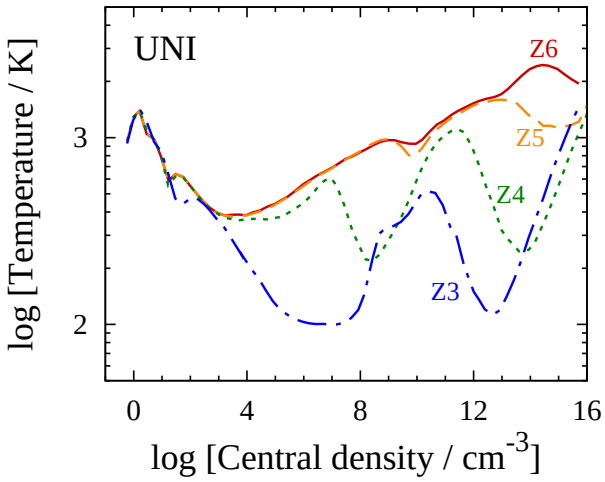

Figure 1. Thermal evolution of the cloud cores of the UNI simulations with metallicities 10^{-6} (Z6), 10^{-5} (Z5), 10^{-4} (Z4), and 10^{-3} $Z_\odot$ (Z3) from top to bottom.

compressional heating and H_2 line cooling. For Z3, the fine-structure line cooling by O I becomes efficient. Thereafter, OH molecules form via the reaction

$$O + H \rightarrow OH + \gamma, \qquad \text{(Reaction 30)}$$

and then OH cooling becomes dominant at $n_H \sim 10^4$–10^8 cm^{-3} for Z3, and 10^6–10^8 cm^{-3} for Z4. The three-body H_2 formation reactions

$$H + H + H \rightarrow H_2 + H, \qquad \text{(Reaction 5)}$$

$$H + H + H_2 \rightarrow H_2 + H_2 \qquad \text{(Reaction 6)}$$

operate at $\sim 10^8$ cm^{-3}, where the exothermic reactions raise the gas temperature rapidly. Then the specific heat ratio temporarily exceeds the critical value of 4/3 for gravitational collapse. Then a pressure-supported core surrounded by accretion shock is formed for Z3. The gas temperature continues to increase to $\sim 10^{11}$ cm^{-3} while the H_2O molecules act as a main coolant. The H_2O molecules are formed via the reactions

$$OH + H_2 \rightarrow H_2O + H. \qquad \text{(Reaction 24)}$$

For Z5, H_2O cooling is a dominant cooling process in a narrow range of density around 10^{10} cm^{-3} as shown by the cyan dashed curve in Figure 2. The gas fragments into two clumps by efficient OH cooling for Z3 as we see in detail in Appendix A1.

Dust cooling becomes efficient at 10^{11}–10^{13} cm^{-3} for Z3, and at slightly larger densities 10^{12}–10^{14} cm^{-3} for Z4. The grain growth enhances the efficiency of the dust thermal emission for Z3–5. Forsterite grains grow rapidly via the reaction

$$2Mg(g) + SiO(g) + 3H_2O(g) \rightarrow Mg_2SiO_4(s) + 3H_2(g),$$

where (g) and (s) denote the species in the gas- and solid-phases, respectively. The magnesium atoms are eventually exhausted (see the purple dotted line in Figure 2). For Z6, although there is little amount of dust, the temperature drops at 10^{14} cm^{-3} by collision-induced continuum cooling.

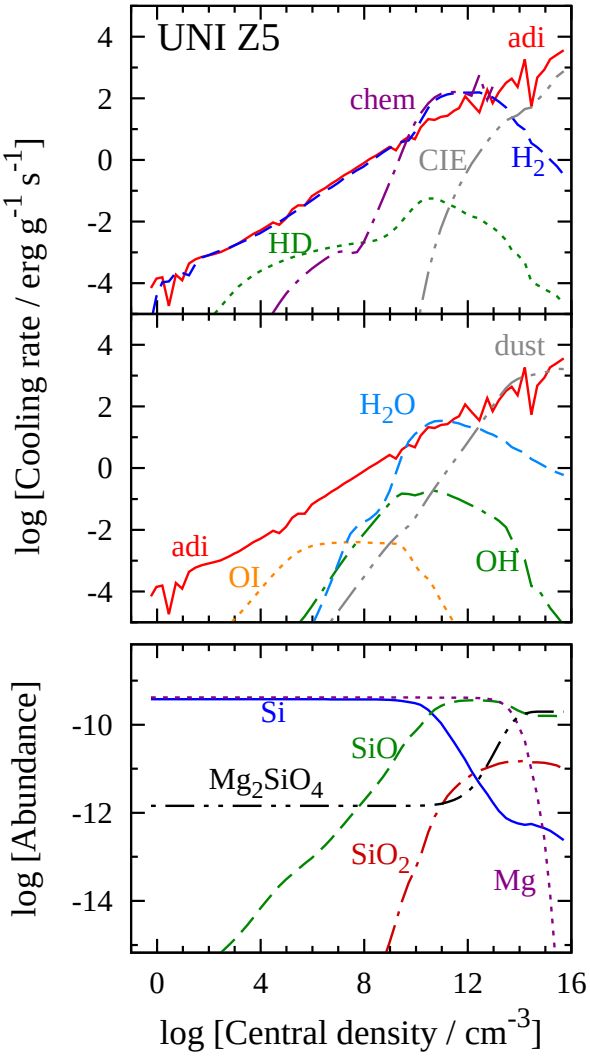

Figure 2. *Top*: cooling functions of primordial species and metal for UNI Z5. The label "adi" depicts the adiabatic compressional heating rate, and "chem" depicts the heating rate owing to H_2 molecule formation. *Bottom*: number abundances of Si atoms (blue solid), SiO molecules (green dashed), SiO_2 molecules (red dot-dashed), Mg atoms (purple dotted), and Si nuclei condensed into Mg_2SiO_4 grains (black dot-dot-dashed) relative to hydrogen nuclei.

Dust cooling becomes ineffective when thermal coupling between the gas and grains is established. The cloud core becomes optically thick soon after this phase, at densities 1×10^{13}, 3×10^{14}, 3×10^{15}, and 1×10^{16} cm^{-3} for Z3, Z4, Z5, and Z6, respectively. The gas pressure rapidly increases in the region where radiative cooling is inefficient due to the large opacity, and then a hydrostatic core bounded by accretion shock is formed. Just inside the shock, the gas disk is formed, being supported by the rotation. As the temperature further increases toward the center, the central part becomes spherical because of the strong pressure support. Here, let us define a pressure-supported "protostar" as the region bounded by a sufficiently spherical iso-density sur-

face.[2] The cloud fragmentation again occurs for Z3 around the time of the first protostar formation. The detailed process is described in Appendix A1.

4 CLOUD FRAGMENTATION

4.1 Thermal evolution and fragmentation of cloud

4.1.1 Overview of the global feature

In order to see whether the gas clouds fragment or not, we follow the evolution over several tens years after the first protostar appears. Figure 3 shows the snapshots output at the time t_* after the first protostar formation. Contrary to the popular notion that cloud fragmentation conditions are largely determined by the gas metallicity, the fragmentation properties are different even with the same metallicity (see panels in each row for a given metallicity). For example, for MH3 Z4, fragmentation does not occur even 30 years after the first protostar formation, while multiple clumps are already formed before the first protostar is formed for MH2 Z4. Clearly, whether a cloud fragments or not is not determined solely by the gas metallicity.

In other words, the thermal evolution, which critically affects the fragmentation property, is not uniquely determined by the gas metallicity. The top panels of Figure 4 shows the temperature evolutions as a function of the central density of four clouds for Z5 and Z4. The evolutionary tracks on the $n_{\rm H}$-T plane vary significantly even with a fixed metallicity. The variation would generate the different fragmentation property as discussed in more detail later. We begin with discussing the physical processes that drive the variation of the thermal evolution in Section 4.2. Then we discuss the effect of the thermal evolution on the cloud fragmentation in Section 4.3. Finally, in Section 4.4, we derive criteria for cloud fragmentation.

4.1.2 Filament fragmentation vs. disk fragmentation

We note an important point that the cloud fragmentation is observed also at a very small metallicity of 10^{-6} $Z_\odot$, where dust cooling is not efficient. For MH1 Z6, the perturbations grow in the spiral arms in a circumstellar disk with a size of $\simeq 10$ AU around the central most massive core. Such a structure is reported also by Clark et al. (2011) and Greif et al. (2012) in the case without metal or dust. Whereas, the simulations with intermediate metallcities 10^{-5}–10^{-3} $Z_\odot$ show a different type of fragmentation. For UNI Z3, MH1 Z4, and MH1 Z5, the "edamame"-like structure, where several protostellar cores are hosted in a long filament extending over $\sim$ 20–100 AU, appears. Such a peculiar structure is formed typically when dust cooling operates, as we discuss later.

Hereafter, we distinguish the former and latter types of fragmentation as *disk fragmentation* and *filament fragmentation*, respectively. Since the disk fragmentation has been discussed in previous numerical studies (Clark et al. 2011; Greif et al. 2012), we in this paper focus on the filament fragmentation, and revisit the disk fragmentation briefly in Section 4.5. The different points between the two types of fragmentation are in more detail discussed in Appendix A3.

4.2 Collapse timescale and the thermal evolution

As described in Section 4.1.1, the thermal evolution has an effect on the cloud fragmentation property even with a fixed metallicity. We find that the different thermal evolution among clouds can be explained by the variation of the collapse timescale. In a slowly collapsing cloud, the adiabatic compressional heating rate per unit volume

$$\Gamma_{\rm adi} = -\rho p \frac{\rm d}{{\rm d}t}\left(\frac{1}{\rho}\right) = \frac{p}{t_{\rm col}} \quad (1)$$

is correspondingly small. Here, $t_{\rm col}$ is the collapse timescale written as

$$t_{\rm col} = \frac{\rho}{{\rm d}\rho/{\rm d}t}. \quad (2)$$

Therefore, the evolutionary track on the $n_{\rm H}$-T plane tends to be located in a low-temperature region.

We measure in our simulations that the time interval over which the peak density increases from $n_{\rm H,peak} = 10^2$ cm^{-3} to 10^{16} cm^{-3} is 3, 4, 11, and 19 Myr for UNI, MH1, MH2, and MH3 Z4, respectively. The cloud UNI contracts most rapidly while the cloud MH3 contracts most slowly among the four clouds. The evolutionary tracks in Figure 4 roughly trace the trend; the temperature of UNI remains high at all densities because of its slow rotation and hence the most rapid collapse. Contrastingly, the temperature of MH3 remains low because the large centrifugal force and the flat distribution of the dark matter slow the gas infall.

4.3 Important thermal processes

Figure 4 shows that different cooling and heating processes become important and characterize the various evolutionary tracks. For example, MH1 and MH3 Z5 enter the regime where dust cooling is efficient at $n_{\rm H} \sim 10^{12}$–10^{14} cm^{-3} while UNI and MH2 do not. In addition to dust cooling, other two cooling and heating processes responsible to the fragmentation can be identified: H_2 formation heating and OH and H_2O cooling. We discuss the processes one-by-one in the following.

4.3.1 Dust cooling

Dust cooling is a crucial process to lower the gas temperature, to promote cloud elongation, and to induce the formation of low-mass fragments at high densities 10^{12}–10^{15} cm^{-3}, where the Jeans mass is small ~ 0.1 $M_\odot$. Figure 4 clearly shows the effect of dust cooling on the filament formation for

[2] In practice, we calculate iso-density contours by dividing the gas into 100 density bins equally separated with a logarithmic scale from $\log(n_{\rm H,peak}) - 3$ to $\log(n_{\rm H,peak})$. Fitting the distribution of the gas particles in each density bin by an ellipsoid with the major- and minor-axes a and b, we obtain the ellipticity $\mathcal{E} = a/b - 1$ of each iso-density surface. We then define the protostellar surface as the least dens (most distant from the center) surface that satisfies $\mathcal{E} < \mathcal{E}_*$ with the critical ellipticity $\mathcal{E}_* = 0.3$. The protostellar mass is only 20% smaller with a smaller threshold of $\mathcal{E}_* = 0.2$.

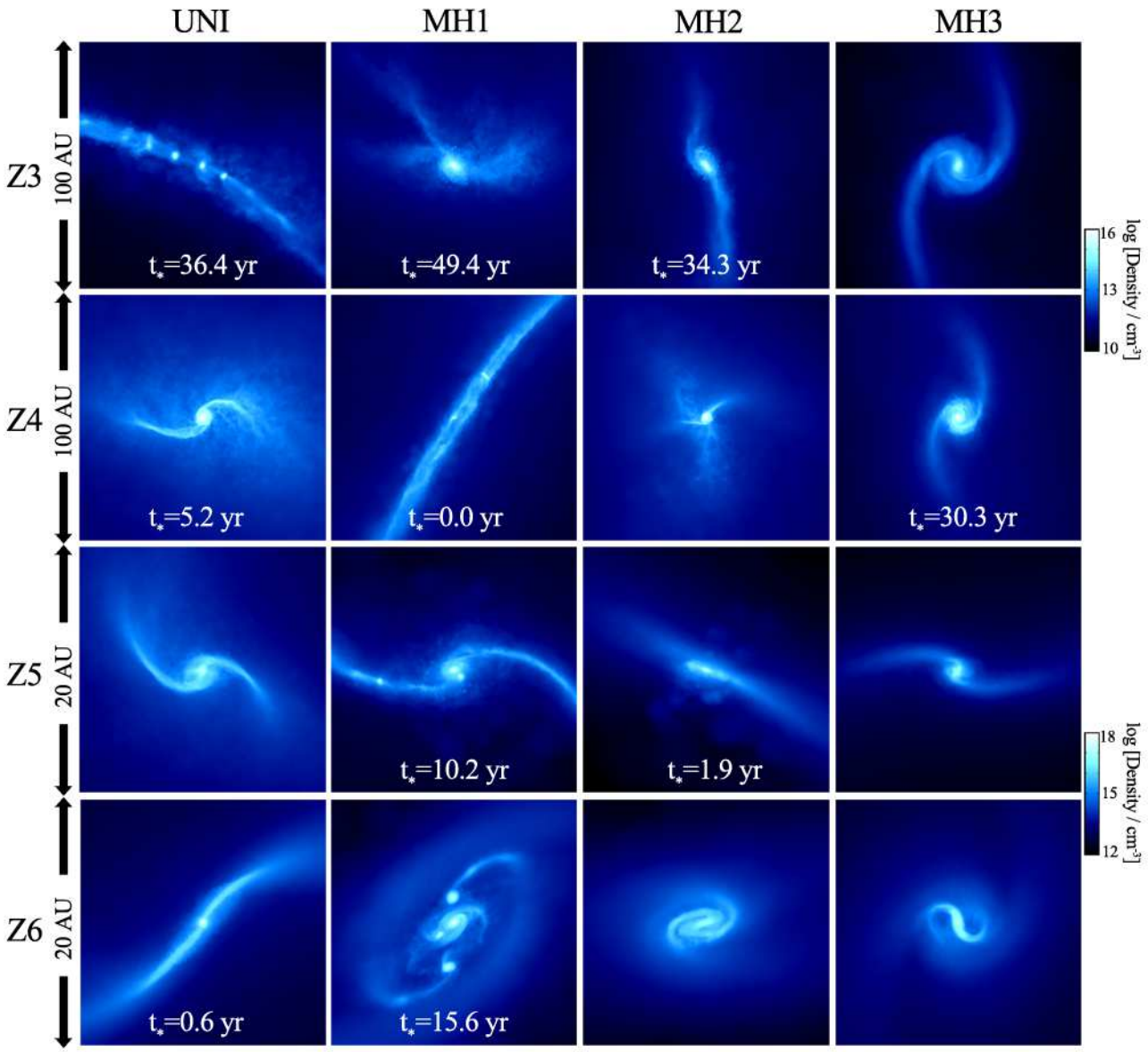

Figure 3. Density-weighted density projection of the clouds UNI, MH1, MH2, and MH3 from left to right with metallicities 10^{-6}, 10^{-5}, 10^{-4}, and 10^{-3} $Z_\odot$ from bottom to top at the time where the simulations are terminated. The plotted region is 100 AU (upper 8 panels) and 20 AU (lower 8 panels) on a side. The color contour depicts the density $n_{\rm H} = 10^{10}$–10^{16} cm^{-3} (upper 8 panels) or 10^{12}–10^{18} cm^{-3} (lower 8 panels) from black to white. These snapshots are output at the time t_* from the first protostar is formed as written in the bottom of each pane. In the models without the time, the central blob does not satisfy our criterion of a protostar (see footnote 2) until the end of the simulation.

MH1 Z4 and Z5. The bottom panels present the cloud ellipticity $\mathcal{E} = a/b - 1$, where a and b are the major- and minor-axes of the cloud. The gas becomes unstable owing to the dust cooling at densities $n_{\rm H} \sim 10^{12}$–10^{14} cm^{-3}, and bar-mode perturbations grow. A filamentary structure is formed as clearly seen in Figure 3. When the ellipticity becomes above 20–30, which is consistent with the critical value defined by Tsuribe & Omukai (2006), the dense filament quickly fragments to yield several protostars.

For UNI and MH2 Z5, even though the temperature decreases slightly by dust cooling at $n_{\rm H} \sim 10^{12}$–10^{14} cm^{-3}, it is insufficient to enhance the ellipticity. The cloud ellipticity increases to only at most 11 and 12 for UNI and MH2, respectively. Figure 3 shows that short filaments are formed in these clouds, but without fragmenting to multiple clumps.

We emphasize that the growth of dust grains further enhances the cooling rate and thus promotes the gas elongation and fragmentation. In the Pop III supernova dust model adopted here, Mg_2SiO_4 grains grow until gas-phase Mg atoms are exhausted at $\sim 10^{14}$ cm^{-3}. Figure 5 (a) compares our simulations with (left) and without (right) grain growth for MH1 Z5 at the same time $t_* = 4.6$ yr after the first protostar formation. While several protostellar cores are born from a filament in the case with grain growth, only a single protostar is formed at the center of a slightly more diffuse filament otherwise.

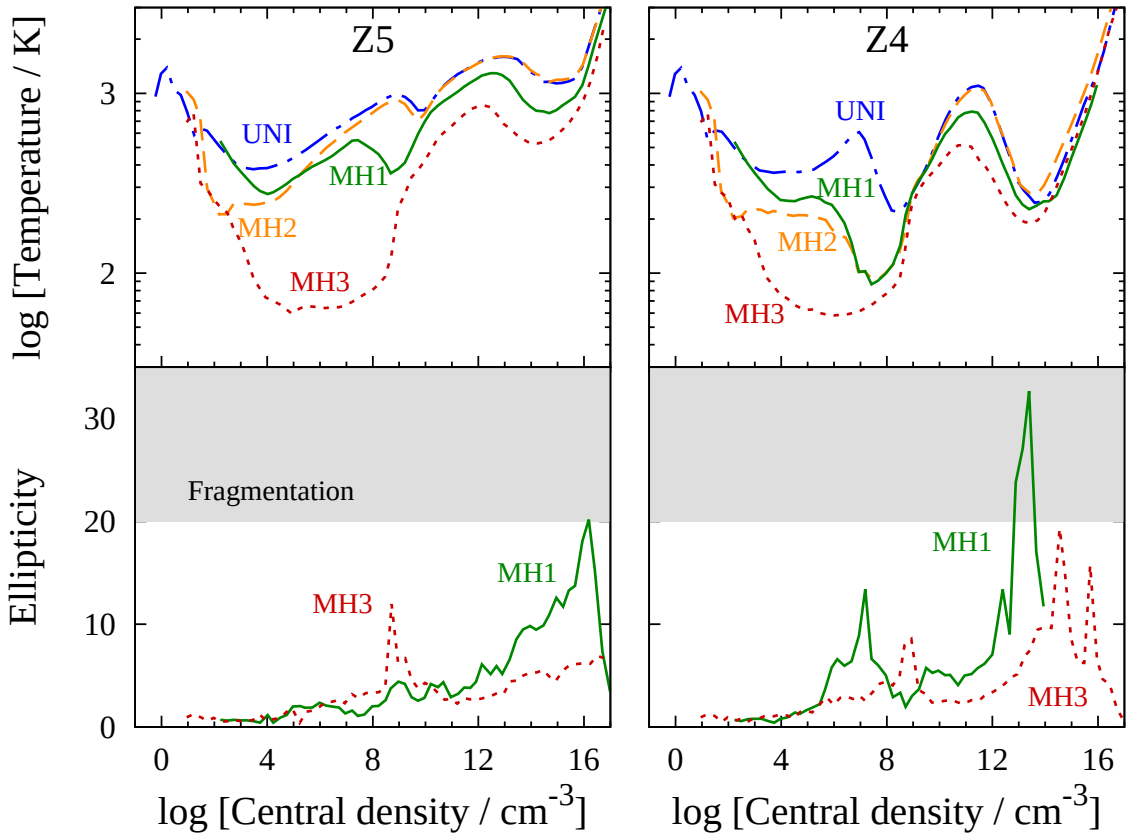

Figure 4. Temporal evolution of the temperature (top) and ellipticity (bottom) as a function of the central density of cloud cores UNI (blue dot-dashed), MH1 (green solid), MH2 (orange dashed), and MH3 (red dotted) for Z5 (left) and Z4 (right). We show the ellipticities only for MH1 and MH3 for clarity. The grey shaded region indicates the ellipticities for which the cloud breaks up into multiple clumps.

4.3.2 H_2 formation heating

In many cases, dust cooling becomes efficient at high densities but the gas cloud does not fragment. We find that chemical heating effectively makes the cloud stable against deformation. For example, in MH3 Z5, the rapid gas heating by the formation of H_2 molecules via three-body reactions becomes efficient at $n_{\rm H} \sim 10^9$–10^{12} cm^{-3}. The temperature rapidly increases from 130 K at $n_{\rm H} = 5 \times 10^8$ cm^{-3} to 700 K at 2×10^{11} cm^{-3}, causing the specific heat ratio to be 1.7 on average, which is sufficient to stabilize the gas against elongation. Then the gas ellipticity rapidly decreases from 12 to 2 as shown in the bottom panel of Figure 4.

The timescale for which the ellipticity increase from such a small value to the critical ellipticity is longer than the dynamical timescale of the cloud. In the clouds UNI, MH1, and MH2 with metallicities 10^{-4}–10^{-3} $Z_\odot$ and in the cloud MH3 with 10^{-6}–10^{-3} $Z_\odot$, the H_2 formation heating significantly suppresses the gas elongation before dust cooling becomes effective to promote the gas elongation.

Tsuribe & Omukai (2008) show that a gas cloud does not fragment with the metallicity range of 10^{-5}–10^{-4} $Z_\odot$, by an order of magnitude smaller than in our simulations. In their present-day dust model predicts 30 times larger efficiency of the H_2 molecular formation on grains than in our Pop III supernova dust model (see Table 2). Hydrogen atoms are exhausted by the formation process before the molecular formation via three-body reactions at $n_{\rm H} \sim 10^8$ cm^{-3}. In their model, H_2 formation heating therefore does not become efficient and can not stabilize the gas. Meanwhile, in our simulations even with 10^{-4}–10^{-3} $Z_\odot$, three-body reactions and the associated gas heating make the cloud rounder.

In order to see the effect more clearly, we perform a controlled simulation without the heating process. Figure 5 (b) shows the density distributions in the central 100 AU region of the cloud MH3 Z4 with (left) and without (right) H_2 formation heating. In the former case, the cloud core ellipticity $\mathcal{E}$ remains around 3 because of the effective chemical heating at $\sim 10^8$ cm^{-3}. In the latter case $\mathcal{E}$ increases up to 15 by OH cooling and then further increases to ~ 30 by dust cooling without any stabilization. Density perturbations in the filament grow and yield several protostellar cores in a thin filament.

4.3.3 OH and H_2O cooling

In the cloud MH1 Z4, although H_2 formation heating is effective (see the green solid curve in Figure 4), a thin filament is formed and quickly fragments to a few clumps. We find that radiative cooling owing to the transition lines of OH and H_2O molecules is important in this case. Figure 6 shows the

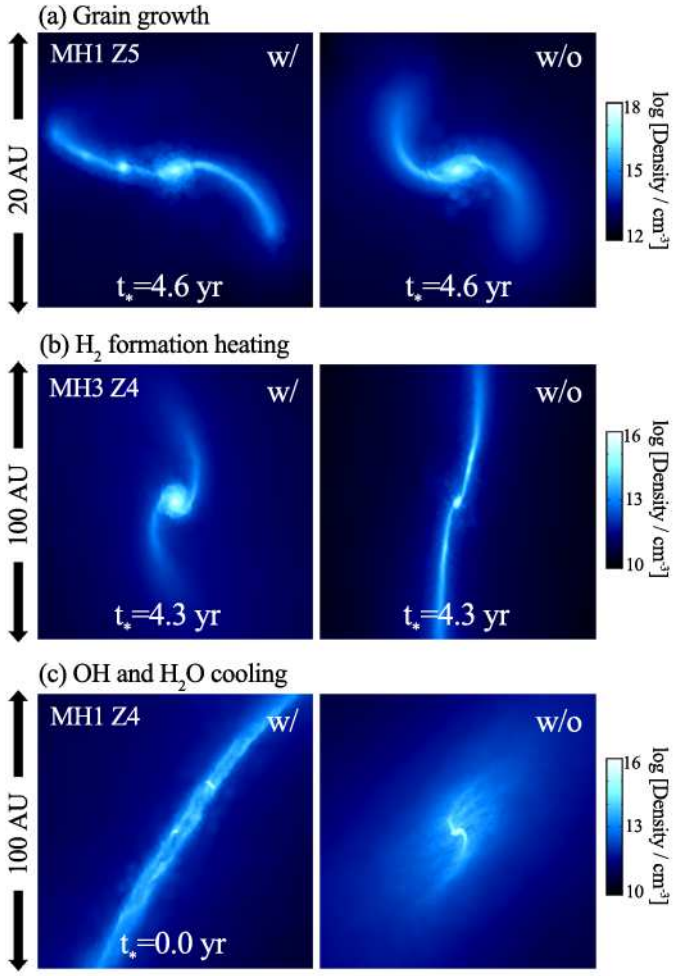

Figure 5. We compare the cloud fragmentation in the regular simulations (left) and controlled simulations (right) at the same epoch. All the relevant chemo-thermal processes are considered in the former simulations, while, in the latter simulations, (a) grain growth, (b) H_2 formation heating, and (c) OH and H_2O cooling are not included.

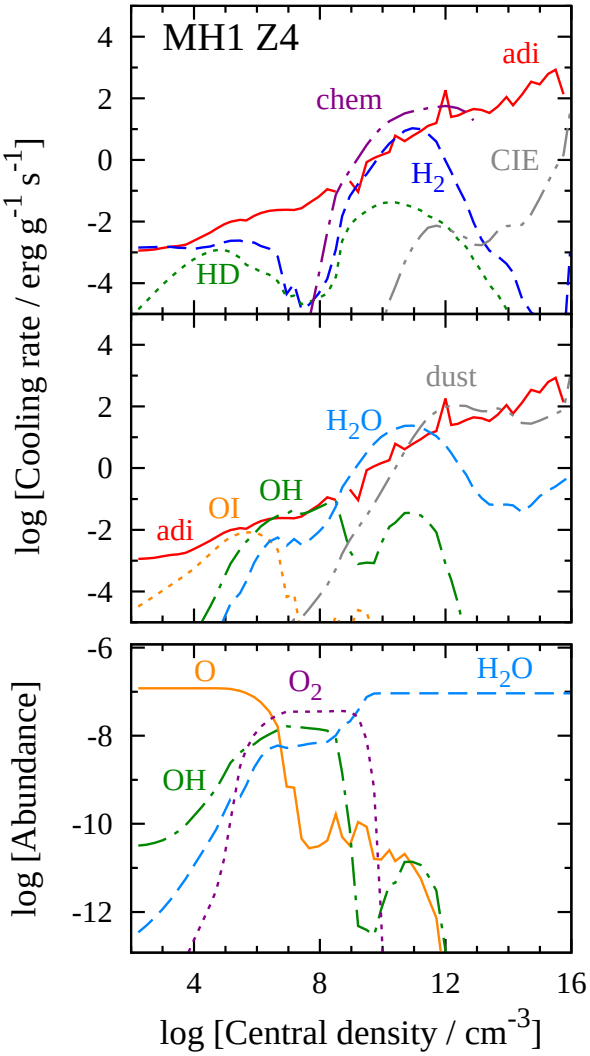

Figure 6. Cooling and heating rates of the dominant processes (top) and the abundances of the O-bearing species (bottom) as a function of the central density for MH1 Z4.

contribution of various heating and cooling processes as a function of density for the cloud. At $n_H = 10^6$–10^8 cm^{-3}, a large fraction of O atoms are converted into OH molecules (green dot-dashed curve), and OH cooling exceeds the adiabatic compressional heating rate (red solid). Even though H_2 formation heating is effective at $n_H \sim 10^9$–10^{11} cm^{-3} and reduces the cloud ellipticity, $\mathcal{E}$ evaluated at 10^{11} cm^{-3} is the largest among the four clouds for Z4 thanks to efficient OH and H_2O cooling. The cloud is then sufficiently elongated to trigger fragmentation. The ellipticity increases up to 33 in the end (see Figure 4). Although H_2O cooling is indeed effective for MH2 Z4 at 10^6–10^8 cm^{-3} (orange dashed curve in Figure 4), it is not sufficient to compensate the stabilization effect by H_2 formation.

Again, in order to see clearly the effect of the OH and H_2O cooling, we perform a controlled simulation without OH and H_2O cooling for MH1 Z4. The result is shown in Figure 5 (c). Without the molecular cooling, even at densities where dust cooling is efficient, a single protostar is formed. Clearly, the efficient OH and H_2O cooling drives the formation of a long filament and subsequent fragmentation. This is for the first time demonstrated by our simulations which explicitly include the metal molecular cooling and the Pop III supernova model with the large oxygen excess.

4.4 Criteria for first low-mass star formation

From the discussion in Sections 4.2–4.3, we can consider that the three thermal processes, dust cooling, H_2 formation heating, and OH and H_2O cooling are important to determine the fragmentation properties of the clouds. Therefore, the criteria for gas fragmentation can be translated into the condition where these processes become effective or not for a given combination of the metallicity Z and the collapse timescale t_{col}. Extending the approach of Schneider & Omukai (2010), we define the fragmentation condition as

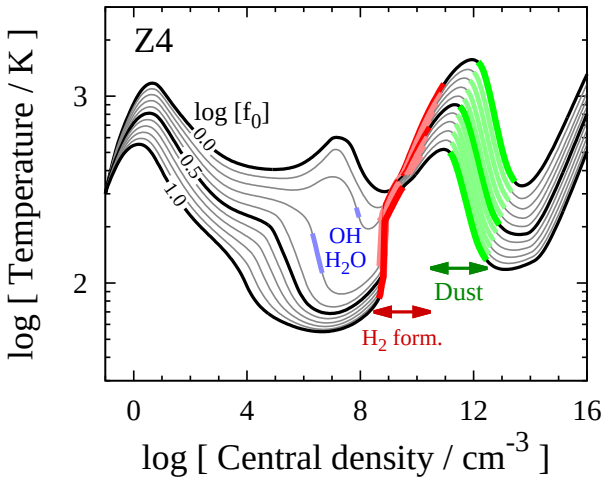

Figure 7. Temperature as a function of the density in a cloud core obtained by the semi-analytic chemo-thermal evolution model of gas clouds for Z4 with f_0 (Equation (3)) from 1 to 10 every 0.5 dex (thick curves) and every 0.1 dex (thin curves). We also draw thick and colored segments in the regimes where $\gamma > 1.1$ by H_2 formation heating (red), where $\gamma < 0.5$ by OH and H_2O cooling (blue), and where $\gamma < 0.8$ by dust emission (green) on each evolutionary track.

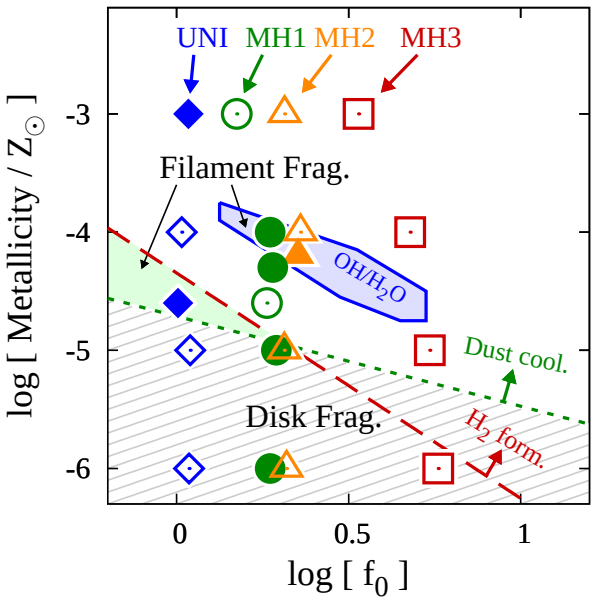

Figure 8. We plot the regions of the collapse timescale f_0 and the metallicity Z favourable for the filament fragmentation (green- and blue- shaded regions) and for the disk fragmentation (grey-hatched region). Dust cooling is efficient in the region above the green dashed lines (labeled "Dust cool."). H_2 formation heating is efficient in the region above the red dotted lines ("H_2 form."). OH and H_2O cooling is efficient in the region surrounded by blue solid line ("OH/H_2O"). We define these lines by linear interpolation of the results of the semi-analytic calculations with varying $f_0 = 1$–10 every 0.05 dex and $Z/Z_\odot = 10^{-6}$–10^{-3} every 0.1 dex. We also over-plot f_0 and Z of the simulated clouds UNI (blue diamonds), MH1 (green circles), MH2 (orange triangles), and MH3 (red squares). Open and close symbols indicate the models that end with and without fragments, respectively.

(i) dust cooling is efficient at high densities $\sim 10^{12}$ cm^{-3} to reduce the specific heat ratio to $\gamma < 0.8$, and

(ii-a) H_2 formation heating is not efficient at intermediate density $\sim 10^8$ cm^{-3}, or

(ii-b) OH or H_2O cooling is efficient so that $\gamma < 0.5$ even though H_2 formation heating later increases γ above 1.1.

The threshold values of γ (0.8, 1.1, and 0.5) used in the above are determined so that the criteria reproduce the results of our simulations. In this section, we aim at defining the region of Z and $t_{\rm col}$ where the gas fragmentation is favored.

There remains a complexity that the collapse timescale itself varies when the cloud collapse proceeds faster/slower owing to gas cooling/heating. We thus introduce a parameter f_0 as an indicator of the collapse timescale that characterizes each cloud. The parameter satisfies the equation as

$$t_{\rm col} = f_0 t^{\rm s}_{\rm col}(\gamma). \quad (3)$$

The factor $t^{\rm s}_{\rm col}(\gamma)$ accounts for the dependence on the specific heat ratio γ, the indicator of the thermal evolution. From the self-similar solution of a polytropic cloud without rotation or dark matter halo, $t^{\rm s}_{\rm col}(\gamma)$ can be written as

$$t^{\rm s}_{\rm col}(\gamma) = \left[\frac{2}{3\pi^2} D_{\rm cen}(\gamma)\right]^{1/2} t_{\rm ff}, \quad (4)$$

where

$$D_{\rm cen}(\gamma) = 4\pi G \rho_{\rm cen}(-t)^2 \quad (5)$$

is the dimensionless form of the density at the center (Yahil 1983; Hanawa & Matsumoto 2000; Lai 2000), and $t_{\rm ff} = (3\pi/32 G\rho_{\rm cen})^{1/2}$ is the free-fall time. $D_{\rm cen}(\gamma)$ increases with the increasing γ for $\gamma > 0.8$, and diverges as γ approaches 4/3. Hereafter, we utilize the parameter f_0 to represent the bulk rate of the cloud collapse.

4.4.1 *One-zone semi-analytic model*

It is costly to run additional three-dimensional simulations which cover a large parameter regions of Z and f_0. We thus resort to utilizing a simpler approach focusing on the chemo-thermal evolution of a cloud. To this aim, the semi-analytic one-zone model of C15 is suitable. We modify the code such that the density in the cloud center increases according to

$$\frac{{\rm d}\rho}{{\rm d}t} = \frac{\rho}{t_{\rm col}} = \frac{\rho}{f_0 t^{\rm s}_{\rm col}(\gamma)} \quad (6)$$

with various f_0.[3] For $\gamma \gtrsim 4/3$ we set the upper limit of $t_{\rm col}$ as $5t_{\rm ff}$, and for $\gamma < 0.5$ we use $t^{\rm s}_{\rm col}(0.5) = 0.32 t_{\rm ff}$. For given density and temperature, our one-zone code solves exactly the same chemical reactions including grain growth and gas heating/cooling processes as in our three-dimensional simulations. The CMB temperature is set to be 50 K (redshift ~ 20). We perform the calculations with varying $f_0 = 1$–10 every 0.05 dex and $Z = 10^{-6}$–10^{-3} Z$_\odot$ every 0.1 dex to cover the parameter range of early clouds.

Figure 7 shows the temperature evolution of the cloud

[3] C15 investigate the cloud evolution only in the case with $t_{\rm col} \simeq 1 t_{\rm ff}$, corresponding to $f_0 \sim 3$.

Table 3. Collapse timescale of clouds f_0.

Z [$Z_\odot$]	UNI	MH1	MH2	MH3
10^{-3}	1.1 ± 0.6	1.5 ± 0.5	2.1 ± 1.5	3.4 ± 1.9
10^{-4}	1.0 ± 0.4	1.9 ± 0.7	2.3 ± 1.4	4.8 ± 2.7
10^{-5}	1.1 ± 0.5	1.9 ± 0.6	2.1 ± 1.5	5.4 ± 2.6
10^{-6}	1.1 ± 0.5	1.9 ± 0.5	2.1 ± 1.6	5.8 ± 2.9

Note — To compute f_0 for the simulated clouds, we measure the collapse time and the specific heat ratio as $t_{\rm col} = \rho/(\Delta\rho/\Delta t)$ and $\gamma = (\Delta T/T)/(\Delta\rho/\rho) + 1$, respectively, where Δx is the difference of the quantity x between a snapshot and its previous snapshot. We arrange the output times such that the maximum density $n_{\rm H,peak}$ of the target cloud increases only 0.25 dex between the two adjacent outputs. We then take the arithmetric mean and the standard deviation of f_0 measured at each output time with $n_{\rm H,peak} < 10^8$ cm^{-3}.

center for Z4 with various values f_0 from 1 to 10 every 0.1 dex. The gas temperature monotonically decreases with increasing f_0 at each density. We find that the evolution track for our simulated clouds (Figure 4) follows closely one of the black curves in Figure 7 with a corresponding f_0 shown in Table 3. We indicate by thick colored segments the regimes where we can identify important thermal processes that determine the cloud elongation and fragmentation. The green segment represents the regime where dust cooling is efficient to reduce γ below 0.8. There, the gas cloud can fragment if the cloud ellipticity is sufficiently large in advance to the rapid gas cooling. The condition is not met if the trajectory passes through the regime colored in red, where significant H_2 formation heating increases γ larger than 1.1. In the limited cases with $f_0 \simeq 1.6$–2.2, we also find that the OH cooling, which is efficient in the blue-colored regions at $n_{\rm H} \sim 10^7$ cm^{-3}, can prevent the gas cloud from recovering a round shape.

We present the results of all our model calculations in Figure 8. The green- and blue-shaded regions indicate the regime where fragmentation criteria are satisfied. There, we also mark the results of our three-dimensional simulations (Table 3). The models that result in fragmentation is indicated by filled symbols, and otherwise by open symbols. The parameter regions for the fragmentation defined by the semi-analytic model are remarkably consistent with the results of the simulations with 10^{-5}–10^{-4} $Z_\odot$. The result for UNI Z3 is not consistent, but this may reflect simply the limitation of our one-zone model to represent the non-linear evolution of hydrostatic core formed by H_2 formation heating.

In Figure 8, the green, red, and blue lines correspond to the boundaries between the models where dust cooling, chemical heating, and molecular cooling, respectively, are effective and not. To draw the boundary curves, we linearly interpolate the critical f_0 and Z obtained by the one-zone calculations. Above the green-dotted line, dust cooling can trigger gas fragmentation (criterion (*i*)). Below the red-dashed line, H_2 formation heating is not effective to suppress the gas elongation (*ii*-a). In the regions surrounded by the blue solid lines, OH and H_2O cooling can enhance the cloud elongation even though the H_2 formation heating is effective above the red-dashed line (*ii*-b). The green-shaded region indicates the parameter region where the criteria (*i*) and (*ii*-a) are both satisfied. In the blue-shaded regions, the fragmentation is favored by the OH and H_2O cooling. Interestingly, our criteria are satisfied in the limited metallicity region $Z \sim 10^{-5}$–10^{-4} $Z_\odot$. In the next section, we explain and derive the boundaries using simple analytic models.

4.4.2 Analytic formulae of the boundaries

Dust cooling

The criterion (*i*) is defined by the balance between the compressional heating rate $\Gamma_{\rm adi}$ and the rate of the heat transfer from gas to dust, $\Lambda_{\rm d}$. From Equation (1), we obtain

$$\Gamma_{\rm adi} = 3.7 \times 10^{-7} f_0^{-1} \ {\rm erg \ cm^{-3} \ s^{-1}}$$

at $n_{\rm H} = 10^{14}$ cm^{-3} and $T = 1000$ K with $t^{\rm s}_{\rm col}(0.8) = 0.27 t_{\rm ff}$. In our Pop III dust model, the dust cooling rate is

$$\Lambda_{\rm d} = 1.8 \times 10^{-7} \left(\frac{Z}{10^{-5} \ Z_\odot} \right) \ {\rm erg \ cm^{-3} \ s^{-1}}$$

when the all of magnesium is depleted onto forsterite grains. Then we obtain the relationship between f_0 and Z where the dust cooling exceeds the gas compressional heating as

$$Z > 2.0 \times 10^{-5} f_0^{-1} \ Z_\odot. \quad (7)$$

With slower collapse, i.e. with larger f_0, the gas compressional heating is less efficient. Then a small amount of metals is sufficient to overcome the gas heating.

H_2 formation heating

The condition where the rapid gas heating by H_2 formation occurs is that the equilibrium temperature $T_{\rm eq}$ at $n_{\rm H} < 10^8$ cm^{-3} is smaller than that at $n_{\rm H} > 10^8$ cm^{-3}. At 10^{11} cm^{-3}, the thermal balance between H_2 formation heating and H_2 line cooling yields $T_{\rm eq} \sim 870$ K. At $n_{\rm H} = 10^7$ cm^{-3}, adiabatic gas compression is a major heating process, whereas the dominant cooling mechanism is H_2 line transition with $Z \lesssim 10^{-5}$ $Z_\odot$, or H_2O line transition with $Z \gtrsim 10^{-5}$ $Z_\odot$. The condition where the equilibrium temperature is less than 870 K at $n_{\rm H} = 10^7$ cm^{-3} is $\Gamma_{\rm adi} < \Lambda_{\rm H_2} + \Lambda_{\rm H_2O}$, where Λ_x is the cooling rate of species x per unit volume. Since these cooling and heating rates are given by

$$\Gamma_{\rm adi} = 2.6 \times 10^{-17} f_0^{-1} \ {\rm erg \ cm^{-3} \ s^{-1}},$$

$$\Lambda_{\rm H_2} = 3.7 \times 10^{-18} \ {\rm erg \ cm^{-3} \ s^{-1}},$$

$$\Lambda_{\rm H_2O} = 7.9 \times 10^{-18} \left(\frac{Z}{10^{-5} \ Z_\odot} \right) \ {\rm erg \ cm^{-3} \ s^{-1}}$$

at 10^7 cm^{-3} and $T = 870$ K with $t^{\rm s}_{\rm col}(1.0) = 0.34 t_{\rm ff}$,[4] the condition can be written as

$$Z > (3.4 f_0^{-1} - 0.47) \times 10^{-5} \ Z_\odot. \quad (8)$$

The boundary is consistent with the red dashed line in Figure 8. For a gas cloud with f_0 and Z above both the red and green lines, we expect that the gas does not get elongated owing to the effect of rapid H_2 formation heating. Hence the filament fragmentation does not occur either when dust

[4] The value corresponds to $D_{\rm cen}(1.0) = 1.67$, the same as the solution of Larson (1969).

cooling is effective. On the other hand, the green shaded region above the green line and below the red line is the regime where the dust cooling is efficient but H_2 formation heating is not (criteria (*i*) and (*ii*-a)). The cloud MH1 Z5 where the fragmentation occurs is plotted in the green region. We explicitly confirm the cloud fragmentation in the additional simulation for UNI with $10^{-4.6}$ $Z_\odot$.

OH and H_2O cooling

The region surrounded by the blue solid lines indicate the regime where OH and H_2O cooling is effective. At $n_H \sim 10^7$ cm^{-3}, OH cooling rate exceeds the compressional heating rate. The rates are

$$\Gamma_{\rm adi} = 6.7 \times 10^{-18} f_0^{-1} \text{ erg cm}^{-3} \text{ s}^{-1},$$

$$\Lambda_{\rm OH} = 3.2 \times 10^{-19} \left(\frac{y({\rm OH})}{0.1 A_{\rm O}}\right) \left(\frac{Z}{10^{-5}\ Z_\odot}\right) \text{ erg cm}^{-3} \text{ s}^{-1}$$

at 10^7 cm^{-3} and 200 K with $t_{\rm col}^{\rm s}(0.5) = 0.30 t_{\rm ff}$, where y(OH) is the abundance of OH molecules relative to hydrogen nuclei, and $A_{\rm O}$ is the oxygen abundance. The condition where $\Gamma_{\rm adi} = \Lambda_{\rm OH}$ can be derived to be

$$Z = 2.1 \times 10^{-4} f_0^{-1}\ Z_\odot. \quad (9)$$

For large f_0 and Z, OH molecules are formed at $n_H < 10^7$ cm^{-3} and $\Gamma_{\rm adi}$ balances $\Lambda_{\rm OH}$ already at 10^7 cm^{-3}. In this case, the gas evolves nearly isothermally without significant temperature drop. Therefore, the condition (*ii*-b) is satisfied in the narrow region around the part of the line given by Equation (9). The blue shaded region with the label "OH/H_2O" indicate the regimes where OH and H_2O cooling promotes the gas elongation. For the combination of f_0 and Z in these regions, the gas cloud eventually fragments by dust cooling even though H_2 formation heating is efficient (criteria (*i*) and (*ii*-b)). The cloud MH1 Z4 (discussed in Section 4.3.3) is in the blue-shaded region, where the OH cooling enhances gas elongation (Figure 4), and gas fragmentation is finally triggered (Figure 3). Also for MH2 with $10^{-4.2}$ $Z_\odot$, the clouds are sufficiently elongated to fragment.

4.4.3 Fraction of low-mass star-forming clouds

It is interesting to ask the number fraction of the clouds that yield fragments. In order to know this, a distribution of the collapse timescale of low-metal gas clouds is needed. Unfortunately, we can not observationally derive the statistics of the collapse timescale of clouds. Instead, one of the clues may be obtained from the distribution of the collapse timescales of primordial clouds obtained by the cosmological simulations of Hirano et al. (2014). We derive f_0 for 52 primordial clouds and calculate the number fraction of clouds that satisfy our fragmentation criterion indicated in Figure 8 with different metallicities. For $10^{-4.2}$–$10^{-4.7}$ $Z_\odot$, the fractions are $\sim$ 2–4%. Clearly, the metallicity range at which low-mass fragments are formed is limited between $\sim 10^{-5}$ and $\sim 10^{-4}$ $Z_\odot$. Also, the fraction is very few. Considering that we here employ the carbon-normal elemental abundance ([C/Fe] < 1), we argue that the number of low-mass extremely metal-poor stars discovered so far is small (Caffau et al. 2011b), possibly reflecting the stringent constraints on the fragmentation of low-metallicity gas clouds.

4.5 Disk fragmentation with $Z \lesssim 10^{-5}$ $Z_\odot$

The fragmentation occurs also for MH1 Z6 although its f_0 and Z are outside the region of the fragmentation condition shown in Figure 8. That is even reasonable because the criteria should not be applied to the cases with

$$Z < 2.0 \times 10^{-5} f_0^{-1}\ Z_\odot, \quad (10)$$

where dust cooling is inefficient (see Equation (7)). Several authors have discussed that low-mass stars are likely to form by the fragmentation on the accretion disks even in the metal-free cases (Clark et al. 2011; Greif et al. 2012; Susa et al. 2014). It can be considered that the fragmentation in their simulations can be categorized in the disk fragmentation.

In the regime, the fragmentation is not triggered by gas cooling but would be triggered by its self-gravity (e.g. Vorobyov & Basu 2010). Gravitational instability of a protostellar disk has been studied extensively (e.g. Gammie 2001). In our simulations, the cloud fragments only for one cloud MH1 Z6 out of five clouds (UNI Z5 and four Z6 clouds) satisfying Equation (10). It might be because of the peculiar density distribution of the MH2 cloud or just because the disk evolution can be followed for the longest time (16 years) among the five clouds. The fragmentation might be observed also for other clouds if we could follow their evolutions for the longer time. Here, we indicate the maximal region favorable to the disk fragmentation as Equation (10) indicated by the grey-hatched area on the f_0-Z plane of Figure 8.

In our cloud MH1 Z6, five gas clumps are formed but all of them immediately migrate into the central primitive protostar with a life time of several years (see Appendix A3). If the formation and migration continue similarly, the mass of the central protostar quickly increases. If some blobs are ejected from the dense disk by multi-body dynamical interactions, they would avoid the merger with the central star and also could no longer accrete the gas from the disk (Zhu et al. 2012; Susa et al. 2014). This would lead the formation of the low-mass stars even in the so-called "hyper metal-poor" regime with metallicities $\lesssim 10^{-5}$ $Z_\odot$.

5 GAS ACCRETION ONTO PROTOSTARS

We have so far discussed the fragmentation condition of the metal-poor clouds. It is worth noting that the gas fragmentation does not immediately mean the low-mass star formation because the protostellar mass increases by the gas accretion after and during the fragmentation. The eventual stellar mass is determined after the entire process of the gas accretion over typically 10^5 years. We follow the gas accretion onto protostars for a limited time (a few tens of years) after the first protostar is formed because we do not employ the sink-particle technique. However, we can accurately follow the process of the gas accretion including the merger of protostellar cores.

We plot the accretion history of the central protostar for MH1 in Figure 9 (see Appendix A2 and A3 for the growth of the secondary protostars for MH1 Z5 and Z6). As for the other clouds, we find that the protostar accretes a larger amount of gas with lower metallicities. We also comment that the mass accretion rate onto the protostar for MH1 is

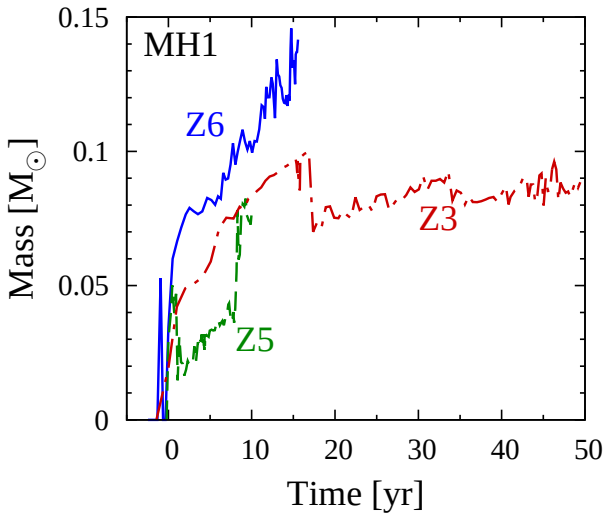

Figure 9. Mass of the protostar first formed in the cloud MH1 for Z3 (red dot-dashed), Z5 (green dashed), and Z6 (blue solid) as a function of the time from the formation of the first protostar.

smaller than for UNI and MH2 even with the same metallicity. This is because the gas temperature remains lower in a slowly contracting gas cloud. Furthermore, the accreting gas is shared by several fragments, and the growth rate of each core is correspondingly reduced.

6 DISCUSSION AND CONCLUSION

The most important conclusion we draw from our set three-dimensional simulations is that not only the gas metallicity Z but also the collapse timescale f_0 determine the thermal evolution and fragmentation "mode" of a contracting gas cloud. Thermal evolution and core fragmentation are intrinsically connected to each other in the following manner:

- The dust thermal emission induces significant deformation of the cloud core. Because accretion of gas-phase metal onto grains enhances the cooling efficiency, it is important to follow the growth of dust grains in a low-metallicity gas.
- Gas heating by H_2 formation via three-body reactions plays a crucial role to halt the elongation of the gas in the cases of vast majority with metallicities 10^{-4}–10^{-3} $Z_\odot$ with the early metal and dust model.
- OH and H_2O gas cooling enhances the cloud elongation and yields favorable conditions for core fragmentation later when dust cooling becomes efficient. In some cases, this occurs before the H_2 formation heating becomes efficient.

We have successfully derived and defined the conditions of filamentary fragmentation on a f_0-Z plane as shown in Figure 8.

It is important to notice that the formation of low-mass fragments does not immediately suggest the formation of low-mass, low-metallicity stars. The final mass of a star when its protostellar evolution reaches the zero-age main sequence is determined the whole history of gas accretion from the circumstellar disk (Shu 1977, 1978; Omukai & Palla 2003; Hosokawa et al. 2011, 2012) starting from a tiny embryo, a protostar, through the growth and contraction. Since the dynamical time becomes progressively small with increasing density as $\propto \rho^{-1/2}$, we are able to follow the gas accretion process only several decades after the first protostar is formed because of technical difficulties. There are a number of important physical processes that affects the growth of a protostar after the initial phase. For example, when the first, central protostar grows to ~ 10 $M_\odot$, photodissociation and photoionization by the ultraviolet emission may become effective to suppress the gas accretion onto the central star (Hosokawa et al. 2012). The magnetic field would also affect the accretion processes (Machida & Doi 2013). Nevertheless, we have shown that the mass accretion rate in early phases is smaller with increasing metallicities. One can naively guess that the fraction of low-mass stars would increase with increasing metallicity.

In a realistic case where the gas is directly enriched by Pop III supernovae, significant turbulence would be generated. Turbulence can suppress the growth of the density perturbation, or rather can even promote gas fragmentation (Dopcke et al. 2011, 2013; Smith et al. 2015). Dopcke et al. (2013) report that small mass fragments (sink-particles) are formed in a turbulent gas for a wide range of metallicities from 0 to 10^{-3} $Z_\odot$. They also find that the mass function of sink particles becomes from flat to bottom-heavy with increasing metallicites between 10^{-5} and 10^{-4} $Z_\odot$. Smith et al. (2015) find vigorous fragmentation of a gas that is enriched with a metallicity 2×10^{-5} $Z_\odot$ by the Pop III supernova exploding in the neighbor halo. The velocity field is coherent over a small length scale of ~ 1 AU in their simulations by the effect of the supernova shocks. Their result supports the notion that turbulence-driven disturbances in a low-metallicity gas induce gas fragmentation. It is still uncertain how the sink particle technique employed in their simulations would affect the fragmentation properties. Further studies are certainly needed to examine the effects of turbulence on gas fragmentation in a fully cosmological set up.

ACKNOWLEDGMENTS

We thank K. Omukai for fruitful discussion. The Pop III dust model is calculated by T. Nozawa. GC and SH are supported by Research Fellowships of the Japan Society for the Promotion of Science (JSPS) for Young Scientists. NY acknowledges the financial supports from JST CREST and from JSPS Grant-in-Aid for Scientific Research (25287050). The numerical simulations are carried out on Cray XC30 at Center for Computational Astrophysics, National Astronomical Observatory of Japan and on COMA at Center for Computational Sciences in University of Tsukuba.

REFERENCES

Aoki, W., Tominaga, N., Beers, T. C., Honda, S., & Lee, Y. S. 2014, Science, 345, 912
Bromm, V., & Loeb, A. 2003, Nat, 425, 812
Caffau, E., Ludwig, H. G., Steffen, M., Freytag, B., & Bonifacio, P. 2011, Sol. Phys., 268, 255
Caffau, E., Bonifacio, P., François, P., et al. 2011, Nature, 477, 67

Caffau, E., Bonifacio, P., François, P., et al. 2012, A&A, 542, A51
Clark, P. C., Glover, S. C. O., Smith, R. J., et al. 2011, Science, 331, 1040
Chiaki, G., Nozawa, T., & Yoshida, N. 2013, ApJ, 765, L3
Chiaki, G., Marassi, S., Nozawa, T., et al. 2015, MNRAS, 446, 2659
Chiaki, G., & Yoshida, N. 2015, MNRAS, 451, 3955
Dopcke, G., Glover, S. C. O., Clark, P. C., & Klessen, R. S. 2011, ApJ, 729, L3
Dopcke, G., Glover, S. C. O., Clark, P. C., & Klessen, R. S. 2013, ApJ, 766, 103
Frebel, A., Aoki, W., Christlieb, N., et al. 2005, Nat, 434, 871
Gammie, C. F. 2001, ApJ, 553, 174
Greif, T. H., Bromm, V.,
Hanawa, T., & Matsumoto, T. 2000, PASJ, 52, 241
Hosokawa, T., Omukai, K., Yoshida, N., & Yorke, H. W. 2011, Science, 334, 1250
Hosokawa, T., Omukai, K., & Yorke, H. W. 2012, ApJ, 756, 93
Hollenbach, D., & McKee, C. F. 1979, ApJS, 41, 555
Hirano, S., & Yoshida, N. 2013, ApJ, 763, 52
Hirano, S., Hosokawa, T., Yoshida, N., et al. 2014, ApJ, 781, 60
Hirano, S., Hosokawa, T., Yoshida, N., Omukai, K., & Yorke, H. W. 2015, MNRAS, 448, 568
Inutsuka, S.-I., & Miyama, S. M. 1997, ApJ, 480, 681
Ji, A. P., Frebel, A., & Bromm, V. 2014, ApJ, 782, 95
Keller, S. C., Bessell, M. S., Frebel, A., et al. 2014, Nature, 506, 463
Lai, D. 2000, ApJ, 540, 946
Larson, R. B. 1969, MNRAS, 145, 271
Matsumoto, T., & Hanawa, T. 2003, ApJ, 595, 913
Machida, M. N., Omukai, K., Matsumoto, T., & Inutsuka, S.-I. 2009, MNRAS, 399, 1255
Machida, M. N., & Doi, K. 2013, MNRAS, 435, 3283
Machida, M. N., & Nakamura, T. 2015, MNRAS, 448, 1405
Nagasawa, M. 1987, Progress of Theoretical Physics, 77, 635
Neufeld, D. A., & Kaufman, M. J. 1993, ApJ, 418, 263
Neufeld, D. A., Lepp, S., & Melnick, G. J. 1995, ApJS, 100, 132
Nozawa, T., Kozasa, T., Umeda, H., Maeda, K., & Nomoto, K. 2003, ApJ, 598, 785
Nozawa, T., Kozasa, T., Habe, A., et al. 2007, ApJ, 666, 955
Nozawa, T., Kozasa, T., & Nomoto, K. 2012, ApJ, 756, L35
Omukai, K. 2000, ApJ, 534, 809
Omukai, K., & Palla, F. 2003, ApJ, 589, 677
Omukai, K., Hosokawa, T., & Yoshida, N. 2010, ApJ, 722, 1793
Pollack, J. B., Hollenbach, D., Beckwith, S., et al. 1994, ApJ, 421, 615
Ritter, J. S., Safranek-Shrader, C., Gnat, O., Milosavljević, M., & Bromm, V. 2012, ApJ, 761, 56
Safranek-Shrader, C., Milosavljević, M., & Bromm, V. 2014, MNRAS, 438, 1669
Safranek-Shrader, C., Milosavljević, M., & Bromm, V. 2014, MNRAS, 440, L76
Santoro, F., & Shull, J. M. 2006, ApJ, 643, 26
Schady, P., Page, M. J., Oates, S. R., et al. 2010, MNRAS, 401, 2773
Schneider, R., Ferrara, A., Salvaterra, R., Omukai, K., & Bromm, V. 2003, Nature, 422, 869
Schneider, R., Omukai, K., Inoue, A. K., & Ferrara, A. 2006, MNRAS, 369, 1437
Schneider, R., & Omukai, K. 2010, MNRAS, 402, 429
Shu, F. H. 1977, ApJ, 214, 488
Shu, F. H. 1978, ApJ, 225, 83
Smith, B. D., Wise, J. H., O'Shea, B. W., Norman, M. L., & Khochfar, S. 2015, MNRAS, 452, 2822
Springel, V. 2005, MNRAS, 364, 1105
Suda, T., Katsuta, Y., Yamada, S., et al. 2008, PASJ, 60, 1159
Susa, H., Hasegawa, K., & Tominaga, N. 2014, ApJ, 792, 32
Todini, P., & Ferrara, A. 2001, MNRAS, 325, 726
Tominaga, N., Iwamoto, N., & Nomoto, K. 2014, ApJ, 785, 98
Truelove, J. K., Klein, R. I., McKee, C. F., et al. 1997, ApJ, 489, L179
Truelove, J. K., Klein, R. I., McKee, C. F., et al. 1998, ApJ, 495, 821
Turk, M. J., Abel, T., & O'Shea, B. 2009, Science, 325, 601
Tsuribe, T., & Omukai, K. 2006, ApJ, 642, L61
Tsuribe, T., & Omukai, K. 2008, ApJ, 676, L45
Umeda, H., & Nomoto, K. 2002, ApJ, 565, 385
Vorobyov, E. I., & Basu, S. 2010, ApJ, 719, 1896
Yahil, A. 1983, ApJ, 265, 1047
Zafar, T., Møller, P., Ledoux, C., et al. 2011, A&A, 532, A51
Zhu, Z., Hartmann, L., Nelson, R. P., & Gammie, C. F. 2012, ApJ, 746, 110

APPENDIX A: DETAIL CLOUD EVOLUTION

We present interesting features in some clouds. For UNI Z3, the cloud fragments in a two-step manner; first by OH cooling and then by dust cooling. For MH1 Z5 and Z6, the secondary protostars infall into the central first protostar.

A1 Two-stage fragmentation for UNI Z3

For the cloud UNI Z3, we observe the fragmentation in the two stages, by OH cooling at $n_{\rm H} \sim 10^9$ cm^{-3} and by dust cooling at $\sim 10^{13}$ cm^{-3}. Figure A1 shows that the cloud is separated into two large clumps (referred to as Clump A and B from left to right) by OH cooling with the separation 2×10^3 AU. The mass of the clumps A and B is 15 and 8 $M_\odot$, respectively. These intermediate-mass clumps further fragment by dust cooling. In Clump A, the density perturbations grow in the filament to form three protostars labeled as A1, A2, and A3, in the order of their formation time. Clump B undergoes monolithic collapse to form a single protostar B1. The mass growth of the protostars is shown in the bottom panel of Figure A1.

We confirm that the transition line cooling can also induce the gas fragmentation as predicted by the several authors (Bromm & Loeb 2003; Frebel et al. 2005; Ji et al. 2014). To be more specific, the relevant cooling agent is OH

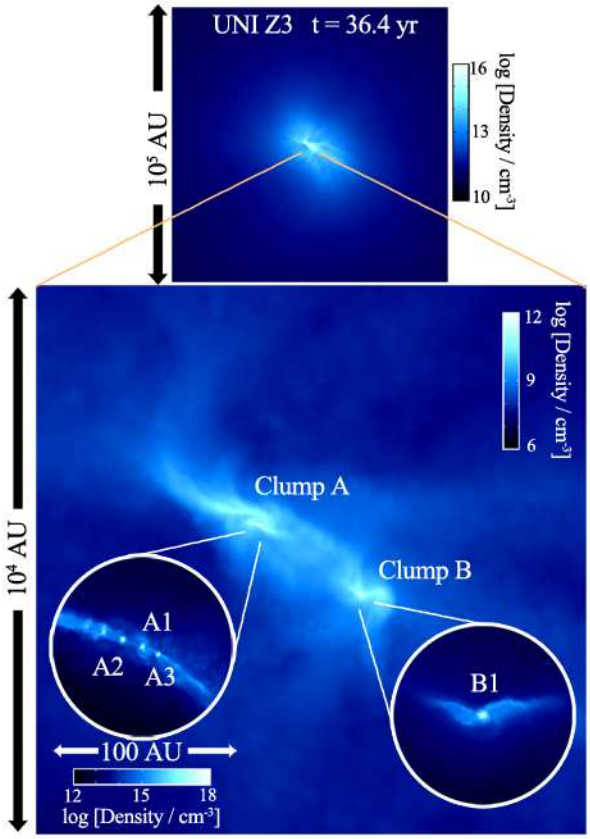

Figure A1. Zoom-in snapshots of the cloud UNI Z3 at 36.4 years after the first protostar formation. The cloud fragments into two clumps owing to the OH molecular cooling, called Clump A and B. The density distributions of Clump A (left) and B (right) within a small volume are shown in the insets. Clump A further fragments into three protostars A1–A3 and further into several sub-clumps owing to dust cooling. Clump B collapses to one protostar called B1.

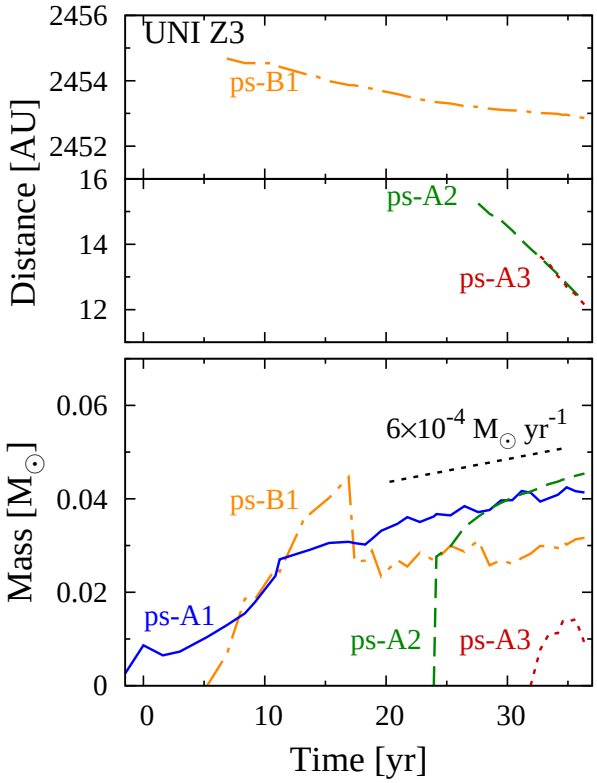

Figure A2. Time evolution of the distance of the secondary protostars from the central protostar (top) and the protostellar mass (bottom) for UNI Z3. In the top panel, the distances of the protostars A2 (green dashed) and A3 (red dotted) are almost overlayed on each other.

molecules, rather than cooling by ions or atoms that the previous studies conclude to be important. Although O I cooling is indeed efficient at the densities 10^2–10^4 cm^{-3} until the level populations reach LTE, the gas temperature does not turn to increase. Since the gas temperature keeps dropping slowly by OH cooling, it does not fragment but continues to be elongated. Fragmentation is triggered only after the OH lines become optically thick and H_2 formation heating becomes efficient at $n_H \sim 10^8$ cm^{-3}, where the Jeans mass is ~ 10 M$_\odot$. Although the mass is still large so that it is unlikely that the star survives until the present-day, and hence they might not be the origin of the Galactic metal-poor stars, the transition line cooling is important to trigger the first-step of the cloud fragmentation.

In Clump A, the cloud enters the second step of the fragmentation at density $n_H \sim 10^{13}$ cm^{-3} where the dust cooling is efficient. In the dense filament, five blobs are formed with similar separations. Three of the five blobs grow to satisfy our criterion of a protostar (footnote 2). In the top panel of Figure A2, we present the distance of the protostars. Protostars A2 and A3 are born at a characteristic distance ~ 15 AU from A1. The linear analysis of an isothermal filament demonstrates that the wave-length of density perturbations most rapidly growing is $\lambda_{\rm max} = 2\pi(2c_s^2/\pi G\rho_{\rm cen})^{1/2}$ (Nagasawa 1987; Inutsuka & Miyama 1997). From the mean density 10^{13} cm^{-3} and temperature 100 K of the filament in Clump A, the length is estimated to be 17 AU. The value is comparable to the initial separation between the protostars in our simulations. After the fragmentation, the mass growth rate of the protostars approaches the common value 6×10^{-4} M$_\odot$ yr^{-1}.

A2 Merger of protostars for MH1 Z5

For MH1 Z5, we see that the secondary protostars quickly merge with the central core. Figure A3 and the top panel of Figure A4 show the projected position and distance of the protostars 2 and 3 from the central most massive core 1, respectively. The protostars 2–4 are born at a distance of ~ 7 AU, comparable to $\lambda_{\rm max}$ at $n_H = 10^{15}$ cm^{-3} and $T = 1000$ K, where the fragmentation occurs. The protostars approach to the center with roughly the infall velocity. Soon after a protostar falls to the center, the next protostar is formed at the similar distance. We can see that the protostar 2 eventually merges with the protostar 1. Then a large mass is added to the protostar 1. The growth rate of the protostar 1 is on average 3×10^{-3} M$_\odot$ yr^{-1} but it abruptly increases when protostar 2 merges with 1. Compared with the accretion rate for UNI Z3, the overall accretion rate is larger by

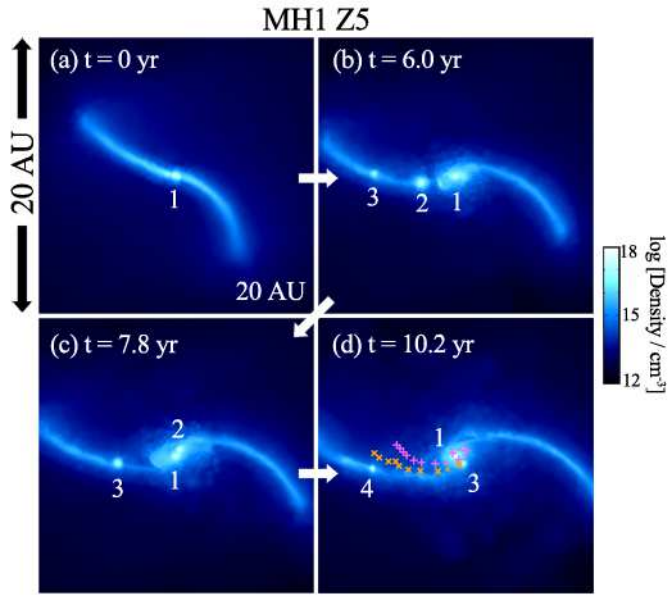

Figure A3. Snapshot of a filament formed through dust cooling in the cloud MH1 Z5 at the time $t_* = 0$ yr (a), 6.0 yr (b), 7.8 yr (c), and 10.2 yr (d) from the formation of the first protostellar core. The protostars "1", "2", "3", and "4" are numbered in the order of their formation. In the panel (d), we also plot the orbits of the protostars 2 (purple plus) and 3 (orange cross) with large symbols at every 0.5 yr and small symbols at every 0.25 yr.

an order of magnitude. This is because the temperature is larger with the smaller metallicity for the smaller efficiency of grain growth and thermal emission of dust grains.

A3 Disk fragmentation for MH1 Z6

Only for MH1 Z6, we can see the disk fragmentation in the several apparent spiral arms. Figure A5 shows the evolution of the accretion disk after the first protostellar core formation. The fragments on the disk have different features from the fragments in the filament fragmentation regime. First, we see that the five more blobs are formed at various distances to the central core while the protostars are formed in the filament fragmentation regime at a fixed distance $\lambda_{\rm max}$ (see Figure A1). Also, the fragments are born with a rotational velocity larger than the radial orbital velocity. Although the protostars in MH1 Z5 eventually have circular orbits just before the merger, their infall is dominated by the radial velocity at the birth time. Further, it is interesting that none of these blobs satisfy our criterion for the protostar defined in Section 5. The gas clumps disperse with irregular shapes while the protostars in the filament fragmentation regime have mostly spherical shapes.

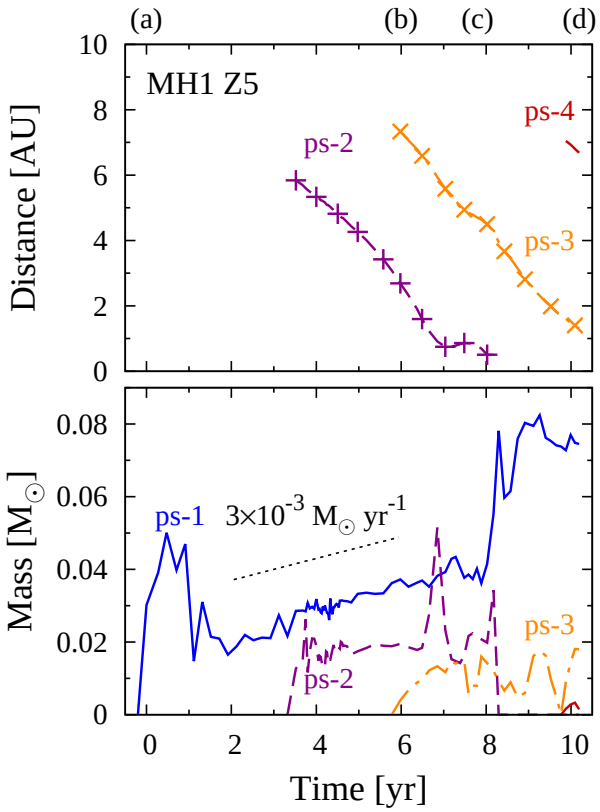

Figure A4. Same as Figure A2 but for MH1 Z5. The plus and cross symbols are attached at the same epochs as shown in Figure A3 (d). The number attached to each protostar and the epochs (a)–(d) correspond to ones in the top panel.

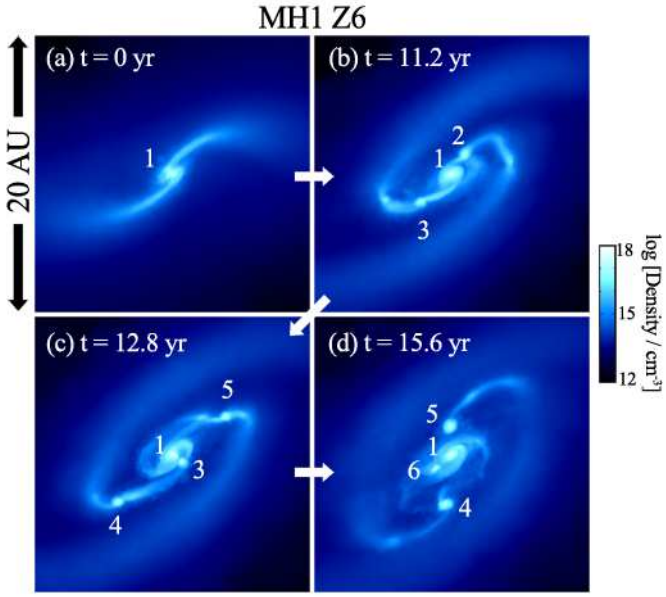

Figure A5. Same as Figure A3 but for MH1 Z6 at the time $t_* = 0$ yr (a), 11.2 yr (b), 12.8 yr (c), and 15.6 yr (d) from the formation of the first protostellar core.